



Uniaxial-strain mechanical detwinning of CaFe_2As_2 and BaFe_2As_2 crystals: Optical and transport study

M. A. Tanatar,^{1,*†} E. C. Blomberg,^{1,2} A. Kreyssig,¹ M. G. Kim,^{1,2} N. Ni,^{1,2} A. Thaler,^{1,2} S. L. Bud'ko,^{1,2} P. C. Canfield,^{1,2}
A. I. Goldman,^{1,2} I. I. Mazin,³ and R. Prozorov^{1,2,*‡}

¹Ames Laboratory, Ames, Iowa 50011, USA

²Department of Physics and Astronomy, Iowa State University, Ames, Iowa 50011, USA

³Naval Research Laboratory, Code 6390, Washington, DC 20375, USA

(Received 10 March 2010; revised manuscript received 17 April 2010; published 11 May 2010)

The parent compounds of iron-arsenide superconductors, AFe_2As_2 ($\text{A}=\text{Ca}, \text{Sr}, \text{Ba}$), undergo a tetragonal to orthorhombic structural transition at a temperature T_{TO} in the range 135–205 K depending on the alkaline-earth element. Below T_{TO} the free standing crystals split into equally populated structural domains, which mask intrinsic, in-plane, anisotropic properties of the materials. Here we demonstrate a way of mechanically detwinning CaFe_2As_2 and BaFe_2As_2 . The detwinning is nearly complete, as demonstrated by polarized light imaging and synchrotron x-ray measurements, and reversible, with twin pattern restored after strain release. Electrical resistivity measurements in the twinned and detwinned states show that resistivity, ρ , decreases along the orthorhombic a_o axis but increases along the orthorhombic b_o axis in both compounds. Immediately below T_{TO} the ratio $\rho_{b_o}/\rho_{a_o}=1.2$ and 1.5 for Ca and Ba compounds, respectively. Contrary to CaFe_2As_2 , BaFe_2As_2 reveals an anisotropy in the nominally tetragonal phase, suggesting that either fluctuations play a larger role above T_{TO} in BaFe_2As_2 than in CaFe_2As_2 or that there is a higher temperature crossover or phase transition.

DOI: [10.1103/PhysRevB.81.184508](https://doi.org/10.1103/PhysRevB.81.184508)

PACS number(s): 74.70.Dd, 72.15.-v, 68.37.-d, 61.05.cp

I. INTRODUCTION

The parent compounds of high-transition temperature, T_c , iron arsenide superconductors, $R\text{FeAsO}$ (R stands for rare earth)¹ and AFe_2As_2 ($\text{A}=\text{Ca}, \text{Sr}, \text{Ba}$, we denote compounds as A122 in the following)^{2,3} undergo a tetragonal to orthorhombic structural transition upon cooling below a transition temperature, T_{TO} , accompanied or followed by an antiferromagnetic (AFM) ordering at T_M .⁴ In free-standing single crystals, this transition leads to the formation of twin domains of four types.^{5,6} In $\text{Ba}(\text{Fe}_{1-x}\text{Co}_x)_2\text{As}_2$, T_{TO} decreases with increasing x and reaches T_c for $x \approx 0.063$.⁷⁻⁹ For a range of dopings twin domains coexist with superconductivity and strongly affect it.^{8,10} While the structural anisotropy (the ratio of the in-plane lattice parameters, a/b) is very small, the electronic structure in the AFM phase is highly anisotropic, as manifested in the first-principles calculations¹¹⁻¹⁴ and in the experiment.¹⁵ In particular, the Fermi surface lacks even approximate fourfold symmetry. At the same time, despite a dramatic anisotropy in the Fermi-surface geometry, calculations predict a rather small transport anisotropy (see discussion below). Intrinsic strong anisotropy is a key component in a popular theoretical picture of “nematic” antiferromagnetic state (see review Ref. 16 for a discussion), which is believed to be incipient even outside the long-range-ordered antiferromagnetic phase and probably plays an important role for superconductivity.¹⁶⁻¹⁹ Yet, experimentally it has not been accessible till now because of the twinned domain structure masking the internal anisotropy. Therefore, it is important to reliably obtain and characterize textured or even better, single-domain samples of these materials.

The fact that T_{TO} is below room temperature makes the situation very different from the classical case of the cuprate $\text{YBa}_2\text{Cu}_3\text{O}_{7-\delta}$, where single orientations of the orthorhombic domains can be stable during sample handling and over the

entire experimental temperature range studied.²⁰ Therefore different approaches are needed to reach a single-domain state. The first attempt to study intrinsic in-plane anisotropy in the iron arsenides was utilizing a strong magnetic field to align domains,²¹ similar to the effect used for turning La_2CuO_4 into a single-domain state.²² The application of a magnetic field of 14 T led to a change in the domain patterns in $\text{Ba}(\text{Fe}_{1-x}\text{Co}_x)_2\text{As}_2$ ($x=0.016$ and 0.025) and in sample with $x=0.025$ lead to an increase of one of the populations by 7% (from 54% to 61%). This resulted in a nonsinusoidal angular dependence of the magnetoresistance with a magnitude of several percent and, because of a small population imbalance, was taken as a signature of large in-plane resistivity anisotropy.

Here we report nearly complete reversible mechanical detwinning in the parent compounds CaFe_2As_2 and BaFe_2As_2 . We used uniaxial strain to drive a region of the crystal into a single-domain state and study the temperature dependence of its electrical resistivity. In both CaFe_2As_2 and BaFe_2As_2 we find a clear effect of detwinning on the resistivity below T_{TO} , with a resistivity decrease along the orthorhombic a_o direction and an increase along the b_o direction. Here and below we use the notations where $a_o > b_o$ so that the ferromagnetic (FM) chains run along b_o . That is to say, the observed anisotropy is not only *much smaller* than one may anticipate from a naive orbital-ordering picture but also the *sign* of the anisotropy is opposite to what one could expect: the electrons move easier along the antiferromagnetic direction than along the ferromagnetic one. Interestingly, both these results also appear in the first-principles calculations.

The ratio ρ_{b_o}/ρ_{a_o} is maximal right below T_{TO} and is larger in Ba122 than in Ca122 (1.5 vs 1.2). Despite the fact that the magnetic moment and the degree of orthorhombicity are increasing upon cooling, the transport anisotropy is *decreasing*.

We discuss possible explanation of this anomalous behavior below.

Finally, the resistivity of Ba122 but not of Ca122 shows measurable anisotropy for at least 30 K above T_{TO} , reflecting nematic fluctuations above T_{TO} (Ref. 23) in the former compound, consistent with the fact that the phase transition in Ca122 is strongly first order and in Ba122 second order or close to that.

II. METHODS

A. Experimental

White light, optical images were taken at temperatures down to 5 K using a polarization microscope Leica DMLM equipped with the flow-type ^4He cryostat, as described in detail in Ref. 5. High-resolution static images were recorded. The spatial resolution of the technique is about $1\ \mu\text{m}$. Single crystals of Ca122 were grown from Sn flux as described elsewhere.^{24,25} Single crystals of Ba122 were grown from FeAs flux.⁷

As schematically shown in Fig. 1, panels (a) and (b), four types of domains are formed in the orthorhombic phase due to orientational degeneracy of the direction of orthorhombic distortion.⁵ Since domains $O1$ and $O2$ (and similarly $O3$ and $O4$) share a common plane corresponding to the tetragonal (100) [or, equivalently (010) plane], their formation does not require lattice deformation and they easily form pairs. This leads to a slight deviation of the orthorhombic axes in the pair from perfectly mutually orthogonal orientation, by an angle $\pm\alpha = \pi/2 - 2\arctan(b/a)$. For resistivity anisotropy study, it is important that domains with two orthogonal orientations of orthorhombic a_o axis are pairwise intermixed, averaging the in-plane anisotropy in the twinned state.

Straining the crystal along the tetragonal $[110]$ directions (that become orthorhombic a_o or b_o axes in the orthorhombic phase) removes the degeneracy and leads to preferential orientation of domains with the a_o axis along the strain. Technically, this requires application of strain at 45° to the natural tetragonal $[100]$ and $[010]$ facets of the crystal.²⁶ Due to both very clean natural growth faces and difficulty to form a good cleave surface, in our initial attempt to detwin samples of CaFe_2As_2 we used as-grown samples. Mechanical strain was applied to the sample through thick silver wires ($125\ \mu\text{m}$ thick), soldered with tin-based alloy²⁷ to the corners of the sample. Use of silver wires to transmit the strain allows for a gentler sample deformation, which is very important for a material as soft as CaFe_2As_2 . It also allows electrical contact to the sample for electrical resistivity measurements. The strain was applied by mechanically deforming a brass horseshoe with a stainless screw, Fig. 1(c), at room temperature. The wires were soldered to the prestrained horseshoe so that both strain and a little stress (due to wire stiffness) could be applied.

The domain population of the BaFe_2As_2 sample has been analyzed by high-energy x-ray diffraction. Entire reciprocal planes were recorded using the method described in detail in Ref. 28 which has been successfully applied recently to study the domain structure in pnictides.^{5,8} The absorption length of the high-energy (99.3 keV) x rays from the syn-

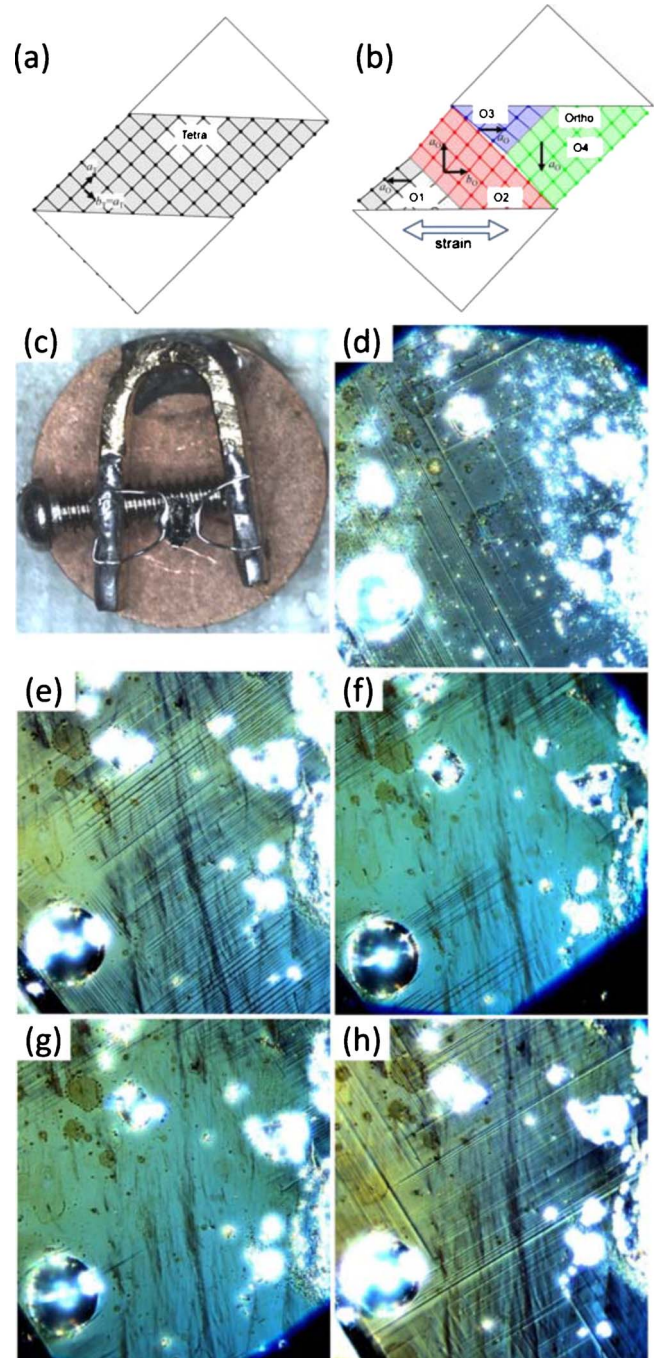


FIG. 1. (Color online) [(a) and (b)] Schematics of domain formation during tetra-ortho transition. Orthorhombic phase is realized through displacement of atoms along the diagonal of the tetragonal lattice with doubling the unit-cell volume and 45° rotation of the crystallographic axes (Ref. 25). The domains are distinguished by the direction of the distortion, a_o , shown for four domains with the arrows. (c) A single-crystal sample of CaFe_2As_2 , mounted on a horseshoe. [(d)–(h)] Polarized light image of the crystal without external strain (d), strained to a progressively higher values [(e)–(g)], and after strain release (h).

chrotron source (beamline 6ID-D in the MUCAT sector at the Advanced Photon Source, Argonne) was about 1.5 mm. This allowed full penetration through the roughly 0.3-mm-thick sample mounted with its c direction parallel to the in-

cident x-ray beam, which was reduced to 0.2×0.2 mm² size by a slit system. Therefore, each single measurement averages over the entire sample *volume* selected by the beam dimension in the **(ab)** plane and its projection through the sample along the **c** direction. The direct beam was blocked by a beam stop behind the sample. Two-dimensional scattering patterns were measured by a MAR345 image-plate positioned 1730 mm behind the sample. During the recording, the sample was tilted through two independent angles, μ and η , perpendicular to the incident x-ray beam by 3.2° .

B. Theoretical

First-principles calculations were performed using the standard linear augmented plane wave (LAPW) method as implemented in the WIEN2K package.²⁹ The experimental lattice and internal parameters were used for both compounds. In order to estimate the transport anisotropy within the constant relaxation-time Boltzmann approximation, we have calculated the anisotropic plasma frequency, $\omega_{p\alpha}^2 = 4\pi\langle Nv_\alpha^2 \rangle$, where N is the density of states per unit volume, $\alpha = x, y$ (with x along a_o direction), v_α is a projection of the Fermi velocity, and the brackets denote averaging over the Fermi surface. Up to 70 000 k points in the Brillouin zone have been used to perform this averaging.

To test the sensitivity of the results, we have performed calculations in both local-density approximation (LDA), with smaller magnetic moments and larger Fermi surfaces, and generalized gradient approximation (GGA), with larger magnetic moments and smaller Fermi surfaces.

III. RESULTS

A. Detwinning

The series of pictures in Fig. 1 show polarized optical images of the Ca122 sample, taken at 5 K, in the area between the contacts without external strain (d), at progressively increasing strain, [(e)–(g)], and after strain release (h). On the application of strain the domain pattern in the central area between contacts changes rapidly and eventually a domain free region is formed. However, a pattern of randomly oriented domains is still seen away from the central part, reflecting the distribution of strain over the sample area and its concentration close to the soldered contacts. Strain release restores the domain pattern, i.e., detwinning is reversible.

Encouraged by this initial success, we introduced two modifications into the sample detwinning process. First, samples were cut into strips to allow a homogeneous distribution of strain between contacts. The image of the sample after cutting, Fig. 2(a), reveals a pattern of random domains, as is typical for an unstrained sample. Second, we attached contacts in a conventional four-probe configuration. The thick wire contacts were made at the ends of the sample and served as current contacts. The potential leads were made from a much thinner, and thus less rigid, 50 μm silver wire long enough to avoid generation of additional strain. The potential contacts were mounted on the rear surface of the crystal so that we could monitor the detwinning in a polarized optical microscope. Figure 2(b) shows an optical image

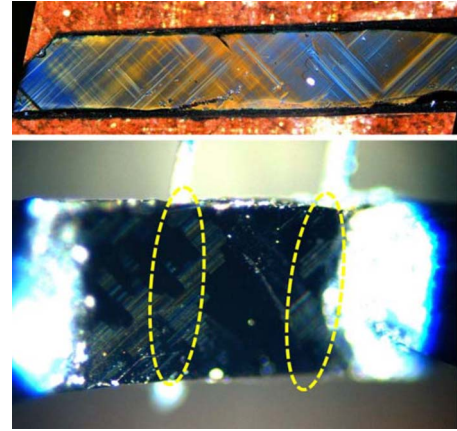


FIG. 2. (Color online) A polarized light image (5 K, $T \ll T_{\text{TO}}$) of a single-crystal strip of CaFe_2As_2 cut along the tetragonal $[110]$ direction before contacts were made (top). The sample was mounted in a usual four-probe contact configuration with potential contacts located on the sample surface opposite to the surface in the image. Strain was applied to the sample at room temperature through current contacts and the image was taken at 5 K on a clear surface under the potential contacts. A big single-domain area can be seen between potential contacts, however, large heavily twinned areas are found above the contacts (circles in the image), revealing notable local reduction in strain by surface tension at the contact points.

of a sample strained through current contacts. Although there is a clear change in the domain distribution upon the application of strain, showing that detwinning affects the whole sample thickness,³⁰ two big unstrained areas can be seen in the central region, which corresponds to the areas above the potential contacts on the rear surface. This observation clearly shows that the contacts affect strain distribution in the sample and do not allow homogeneous sample deformation.

In an attempt to further improve detwinning for resistivity measurements, we started sample deformation through potential contacts. In this case only a central part of the sample, between the potential contacts, is deformed. Simultaneously, the parts of the sample between the thin-wire current contacts and the thick-wire potential contacts remain strain free. Imaging of the sample at 5 K during different stages of the sample preparation and straining is shown in Fig. 3. As can be seen in a series of images, the central part of the sample is predominantly free of domains while a clear pattern of domains can be seen in the unstrained part of the sample. The pattern of domains disappears abruptly at T_{TO} , the strained part abruptly changes color at T_{TO} , signaling the disappearance of the orthorhombic distortion. Formation of the orthorhombic phase is homogeneous through most of the sample, except for two small patches close to the contacts.

B. Resistivity of CaFe_2As_2

The left panel of Fig. 4 shows the temperature-dependent electrical resistance, measured on sample A during two successive thermal runs (cooling from 300 to 5 K and warming up to 300 K) in the unstressed (blue curve) and stressed (red curve) states. It is clear that the strain itself is not large

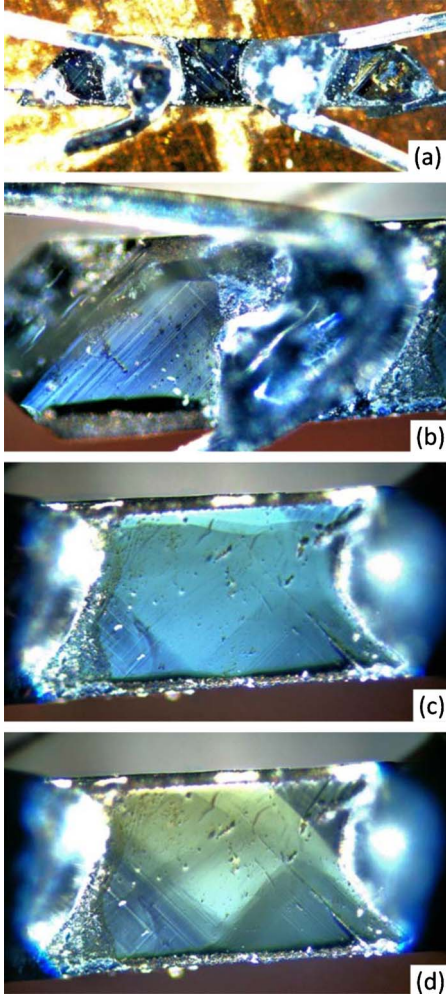


FIG. 3. (Color online) (a) A polarized light image (5 K, $T \ll T_{TO}$) of a single crystalline strip sample of CaFe_2As_2 with soldered contacts before being mounted on a horseshoe. On application of strain in a horizontal direction through the potential contacts, a strain-free area at the left end of the sample remains heavily twinned (b) while the central area turns into a nearly single-domain state, with small twinned areas at the bottom of the image (c). After three thermal cycles from the 300 to 5 K range, strain in the sample is partially released (d), however, large single-domain areas remain, demonstrating the reproducibility of the strain-induced detwinning.

enough to cause a change in the value of the sample resistance at room temperature, beyond a small ($\sim 1\%$) systematic resistance increase on strain change (both increase and decrease) due to a fatigue. The data above T_{TO} stay unchanged, below a clear change in resistance is observed. In particular, the upward jump in the resistivity below T_{TO} is notably diminished in the detwinned state. The data in the unstrained state compare well with the temperature-dependent resistivity in the standard resistance measurements along the $[100]$ direction.^{3,24,31,32} The inset in the left panel shows the same data, normalized by the room-temperature value, in comparison with the data for sample B, measured in the same contact configuration. The data agree very well in the magnitude of the effect. It can be clearly seen that the position of the transition is not shifted with

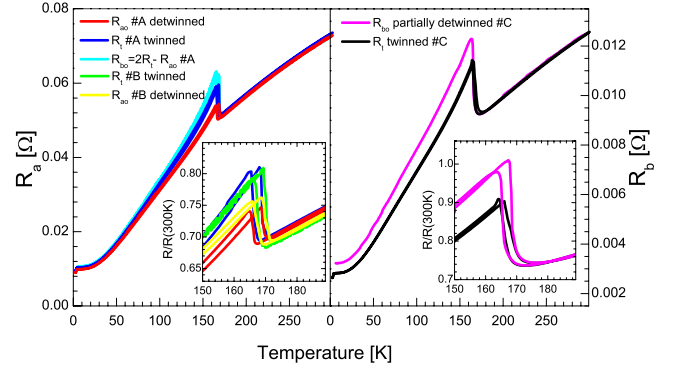


FIG. 4. (Color online) Left panel. Temperature-dependent electrical resistance measured on a sample A of CaFe_2As_2 in twinned (R_t , blue curve) and detwinned (R_{ao} , red curve) states. The third curve is obtained as hypothetical $R_{bo} = 2R_t - R_{ao}$, impossible to measure in the same contact arrangement, see text for details. Inset shows zoom of the transition region for samples A and B, revealing diminishing amplitude of the resistance jump in $\rho_{ao}(T)$ with identical transition sharpness and position. Right panel shows resistance of sample C in which resistivity was measured along b axis in transverse to strain contact configuration (see Fig. 5) in stress-free and stressed (partially detwinned) states. Inset shows zoom of the transition area. This data directly show an increase in the resistance jump in ρ_{bo} .

strain, the transition remains sharp, and the width of the hysteresis between the cooling and warming cycles remains the same. This clearly shows that the transition itself is insensitive to the applied strain and, in view of the strong sensitivity of the transition temperature to uniaxial stress,³¹ the applied strain is very small and homogeneous.

To check if the effects of thermal cycling are important, we took a polarized light image of the sample A after a resistivity run in the detwinned state. The optical image of the sample in a third successive thermal run, following the optical run of Fig. 3(c) and resistivity measurements in Fig. 4, is shown in a panel (d) in Fig. 3. As can be seen, the strain is slightly released after thermal cycling, however most of the sample remains domain free. After this second imaging, the strain in the sample was released and temperature-dependent resistivity measurements were undertaken in a strain-released state, main panel in the left panel of Fig. 4. These revealed a resistivity curve very close to the strain-free samples, restoring the magnitude of the resistivity up-jump to its initial value.

Since the contact configuration in Fig. 3 does not allow for a measurement of ρ_{bo} , we inferred its evolution by assuming that the resistivity in the twinned state is an average of ρ_{ao} and ρ_{bo} . This is strictly true if the population of the domains is random. The calculated $R_{bo}(T) \equiv 2R_t - R_{ao}$ is shown in the left panel. The comparison of $\rho_{bo}(T)$ and $\rho_{ao}(T)$ gives a ratio of 1.2 at the transition. With cooling, the ratio decreases to 1.05–1.1 (due to the small absolute value, the effect of fatigue cannot be neglected and it is hard to place a more precise value on the low-temperature anisotropy).

To get an independent assessment of the $\rho_{bo}(T)$ we have mounted the sample C in such a way that the strain be generated in the direction perpendicular to the current. This was

achieved by soldering the current contacts along the entire side of the rectangular sample and straining the sample and the current contact wires on a horseshoe. The ends of the sample were covered with epoxy glue and glued to two pieces of fiberglass to provide homogeneous deformation (see Fig. 5). The area of the potential contacts was minimized to diminish their effect on the measurements. Sample imaging showed clear detwinning, see Fig. 5, however not in the entire sample. In the right panel of Fig. 4 we show the resistivity obtained in the twinned and partially detwinned states of sample C. The resistivity indeed shows an increase right below T_{TO} . At the same time, the temperature-dependent resistance in the tetragonal phase is unaffected by the strain all the way down to T_{TO} , indicating that there is no residual nematic ordering above T_{TO} , which is, in fact consistent with the fact that the phase transition in Ca122 is strongly first order.¹⁹ Note that since all measurements are taken on the same sample with the same contacts, they are free of any possible geometric uncertainties.

C. Resistivity of BaFe₂As₂

Single crystals of Ba122 were detwinned in the same fashion as Ca122 above, with optical imaging confirming a homogeneous detwinned state for resistivity measurements along the a_o axis and a predominantly detwinned state for resistivity measurements along the b_o axis. Because of small image contrast, samples were additionally studied with high-energy synchrotron x ray as described in the next section.

In Fig. 6 we show the temperature-dependent electrical resistivity of Ba122. The left panel shows the resistance measured along the strain, R_{ao} (sample D), the inset shows the transition area with the data from sample D as well as from another sample, E. The anomaly at ~ 20 K is due to partial superconductivity, typically observed in parent compounds.^{32,33} It appears at temperatures where superconductivity builds up under pressure.³ The authors of Ref. 33 has shown a link between the anomaly and strain in the crystals. In our sample the anomaly becomes more pronounced than in cleaved samples of Ref. 32 due to sample cutting along [110] direction, which easily creates strain along easy cleavage [100] plains. Similar to the case of CaFe₂As₂, we can infer the resistivity of Ba122 along the b_o axis from $R_{bo} = 2R_t - R_{ao}$; the inferred R_{bo} is also shown in Fig. 6. The right panel shows resistivity measurements with current transverse to the strain in the twinned and partially detwinned states on yet another sample F.

Below T_{TO} the data from Ba122 is qualitatively similar to that of Ca122; both show anisotropies right below T_{TO} , of 1.2 (Ca122) and 1.5 (Ba122). In both materials the anisotropy decreases with cooling below T_{TO} , that is to say, is anticorrelated with the degree of orthorhombicity and the long-range magnetic moment. The absolute change in the anisotropy is similar, 10% (from 50% to 40% in Ba122 and from 20% to 10% in Ca122). Note that this similarity holds despite the fact that the residual resistivity in Ba122 is substantially higher—the anisotropy of ρ_0 is also higher. As explained below, this is consistent with the idea that the transport anisotropy reflects the anisotropy of the carrier velocity.

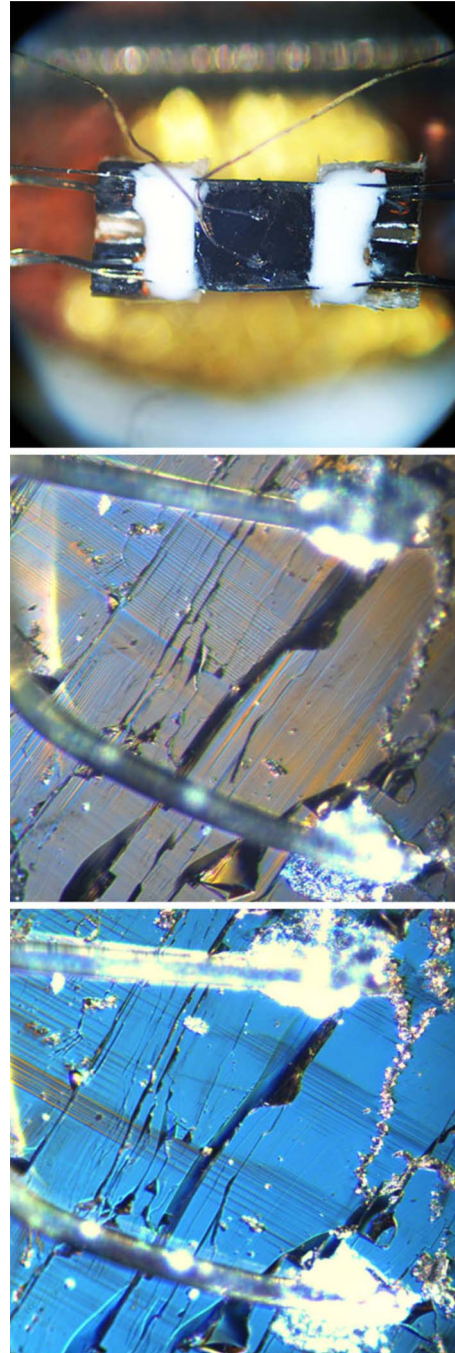


FIG. 5. (Color online) Top panel. Image of the sample for resistivity measurements in transverse to the strain (horizontal) direction. The current contacts are made along the whole length of the top and bottom edges of the sample, right and left sample edges are covered with epoxy glue to provide homogeneous deformation of the sample and wires. Straining force is applied on horseshoe, similar to Fig. 1(c). Potential contacts are made small to minimize the effect on the strain distribution. Middle and bottom panels show area close to potential contacts in stress-free and stressed states.

Another important observation is that in Ca122 the anisotropy drops to 1 right above the transition, reflecting its first order nature, in Ba122 an anisotropy is detectable at least up to 30 K above the transition, a manifestation of strong nematic fluctuations above T_{TO} .²³ This is consistent with the

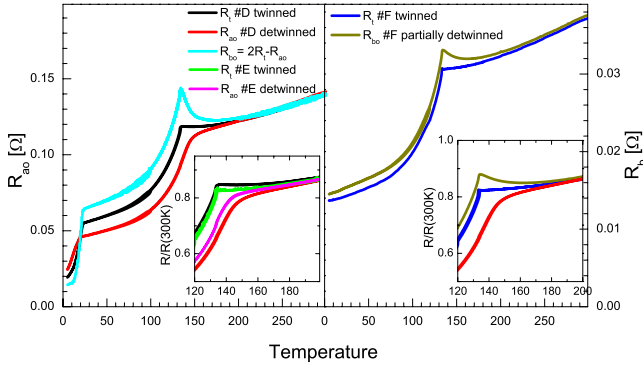


FIG. 6. (Color online) Left panel. Temperature-dependent electrical resistance measured on a sample D of BaFe₂As₂ in twinned (R_t , black curve) and detwinned R_{ao} , red curve) states. The third curve is obtained as hypothetical $R_{bo} = 2R_t - R_{ao}$, impossible to measure in the same contact arrangement. Inset shows zoom of the transition region for samples D and E. Right panel shows resistance for sample F in which resistivity was measured along b axis in transverse to strain contact configuration in stress-free (blue line) and stressed (partially detwinned, yellow line) states. Inset shows zoom of the transition area in normalized resistance plot in comparison with resistance of sample D in the detwinned state.

phase transition in Ba122 being second order or very close to such, which, in turn, was argued to be related to a harder lattice and weaker magnetoelastic coupling in Ba122.

D. X-ray characterization of detwinned state of BaFe₂As₂

The upper panels of Fig. 7 show the splitting of the tetragonal $(220)_T$ reflection into the orthorhombic $(400)_{O1}$ and $(040)_{O2}$ reflections produced by domains $O1$ and $O2$, with different orientations, below the structural transition in a sample area that was nearly strain free. Illuminating the sample with 200 μm diameter x-ray spot at positions between strain-applying contacts yields the pattern shown in the lower panels of Fig. 7. The intensity in the $(400)_{O1}$ reflection is strongly enhanced indicating that the domains with their orthorhombic \mathbf{a} axis ($\mathbf{a} > \mathbf{b}$) along the direction of the applied strain are more populated. The full penetration of the high-energy x-ray beam through the sample allows a quantitative analysis of the bulk domain population with an error of approximately 1% by using the relative intensities in all orthorhombic (400) and (040) reflections.

Scanning the x-ray beam across the sample allows a spatially resolved characterization of the domain population as demonstrated in Fig. 8. Here we show that the sample is nearly detwinned between the contacts, whereas the domain population comes closer to 50% (the value expected for a random distribution of twins) at positions below the contacts, as shown in the right-top pixel in Fig. 8. This confirms our conclusion, Fig. 2, that contacts act as anchors for the deformation.

E. Theoretical analysis

To analyze these results let us write the resistivity in Boltzmann (relaxation-time) approximation, keeping in mind that

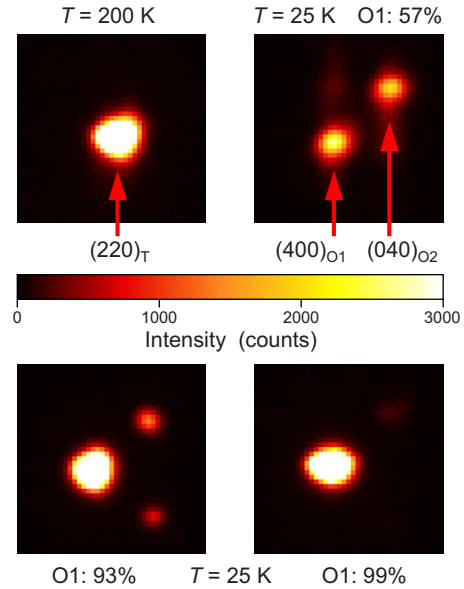


FIG. 7. (Color online) Sections of reciprocal $(HK0)$ planes around the position of the tetragonal $(220)_T$ reflection recorded from the BaFe₂As₂ sample by high-energy x-ray diffraction as described in the text. In the orthorhombic state at $T=25$ K, the $(400)_{O1}$ and $(040)_{O2}$ reflections are related to different domains $O1$ and $O2$, respectively. Analysis of the intensities in pattern recorded at different positions on the sample, below a contact in the upper panels and between the contacts in the lower panels, yield the indicated percent values for the domain $O1$ population bolstered by the applied strain.

the relaxation times for holes and for electrons may be different. Despite the fact that the magnetic structure of A122 compounds is highly anisotropic, we would assume that the relaxation times are isotropic, as we will discuss below (in particular, it is important to keep in mind that the Fermi surfaces, both experimental and calculated, are much smaller in size that the antiferromagnetic vector). Thus, we write

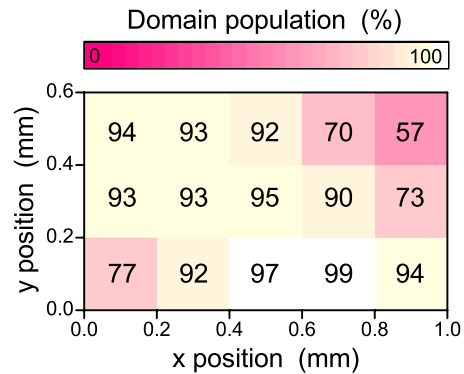


FIG. 8. (Color online) Spatial distribution of the population of $O1$ domains in strained BaFe₂As₂. The population was determined from the relative intensities of the $(400)_{O1}$ and $(040)_{O2}$ peaks, as shown in Fig. 7. The area between the contacts, through which the strain was applied, was probed in 0.2 mm vertical and horizontal steps, determined by the x-ray beam size. The number and color in each pixel correspond to the percent value for the domain $O1$ population. The pixel in the upper right corner corresponds to an area under the contact.

$$1/\rho = 1/\rho_h + 1/\rho_e, \quad (1)$$

$$\rho_i = (4\pi/\omega_{p,i}^2)(1/\tau_{0,i} + 1/\tau_{ph,i} + 1/\tau_{ee,i} + 1/\tau_{mag,i}), \quad (2)$$

where i stands for holes or electrons. The prefactor, ω_p^2 , is the only quantity directly affected by twinning (except for a possible scattering by domain walls in τ_0 that in principle would go away with detwinning; however, the twin domain walls are usually weak scatterers). In the classical Boltzmann theory it is presumed that ω_p^2 and τ_0 are temperature independent, which allows one to separate ρ additively into two terms, a temperature-independent residual resistivity and the temperature-dependent scattering by thermal excitations (phonons, magnons, and electrons). Unfortunately, this is not the case here. The Hall-effect studies found that upon cooling in the AFM phase, the carrier concentration drops drastically, as reflected by the nearly an order-of-magnitude reduction in the plasma frequency, ω_p^2 , and the density of states also decreases substantially (the latter effect makes τ_0 temperature dependent but this is not important for us now).

The standard approximation implies an isotropic relaxation time, even if the bosons providing inelastic scattering are anisotropic. Our first task is to verify whether this remains a good approximation in our case. Given the large magnetic anisotropy and large difference in the ferro- and antiferromagnetic correlation length above T_{TO} (Refs. 34–36) one may think that scattering by the spin fluctuations may be anisotropic as well. To analyze that, let us recall the classical theory of the inelastic transport scattering in solids. The scattering rate for the current flowing in a given direction i is defined by the Fermi golden rule [see, e.g., Ref. 37, Eq. (37)],

$$\frac{1}{\tau_i} \approx A \sum_{\mathbf{k}\mathbf{k}'} v_{\mathbf{k}i}^2 |M_{\mathbf{k}\mathbf{k}'}|^2 \delta(\varepsilon_{\mathbf{k}}) \delta(\varepsilon_{\mathbf{k}'}) / \sum_{\mathbf{k}} v_{\mathbf{k}i}^2 \delta(\varepsilon_{\mathbf{k}}), \quad (3)$$

where A is an isotropic factor, the denominator is proportional to the plasma frequency squared, $M_{\mathbf{k}\mathbf{k}'}$ is the matrix element of the electron-magnon scattering by a magnon with the wave vector $\mathbf{q} = \mathbf{k} - \mathbf{k}'$ and energy $\hbar\omega(\mathbf{q})$, and the cross terms involving $v_{\mathbf{k}}v_{\mathbf{k}'}$ were neglected. The standard argument goes like this: even though the bosons (magnons, in our case) may be much softer, and more easily excited by temperature, in one q direction than in the other, the fact that the scattering processes are integrated twice over the Fermi surface effectively averages out any spectral anisotropy. Moreover, in fact direct neutron measurements^{35,36} show that the magnon dispersions along x and along y differ by less than 15%. Furthermore, small size of the Fermi surfaces in the magnetic state (note that the Hall concentration drops quite rapidly below T_{TO} , indicating that the Fermi surfaces start to shrink immediately below the transition³⁸) only lets the magnons with small \mathbf{q} participate in scattering and at small \mathbf{q} 's the anisotropy of the magnon spectra is particularly low. Thus a strong anisotropy in τ is unlikely, although cannot be excluded.

Let us now analyze the most anisotropic term in Eq. (1), the plasma frequencies. These are intimately related with the electronic structure near the Fermi level, so we show in Fig.

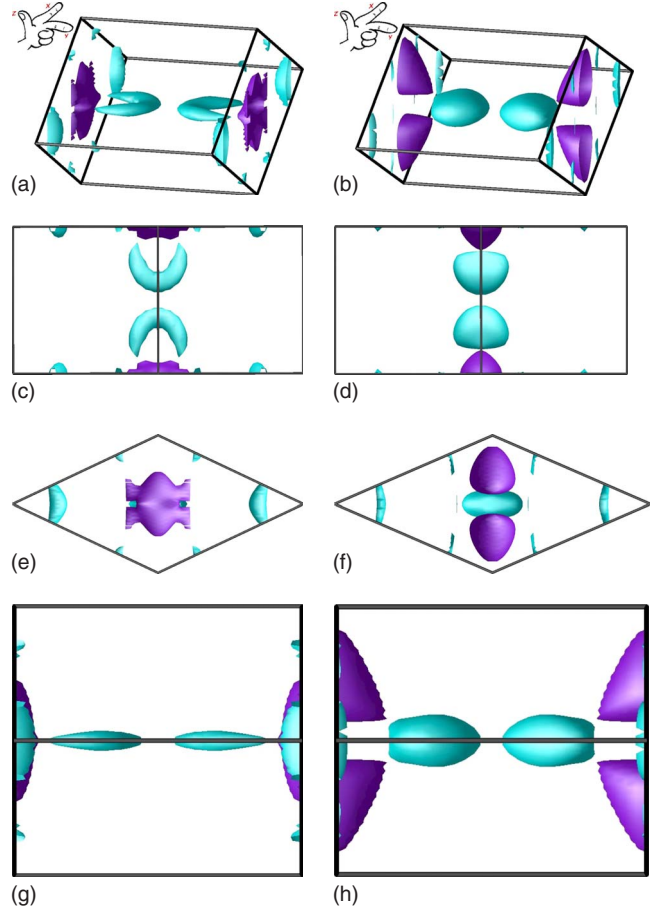


FIG. 9. (Color online) Fermi surfaces for Ca122 (left panels) and Ba122 (right panels), obtained in the LDA band-structure calculation (low magnetic moment). One reciprocal-lattice unit cell is shown, with the Γ points located in the eight corners. The top panels represent a general view (directions of the axes as shown), the next row represents the view from the top, along the k_z direction (k_x - k_y plane), the third row represents the front view, along the k_y direction (k_x - k_z plane), the last row presents the side view, along the x direction (k_y - k_z plane). The light shaded (cyan) surfaces are electron pockets, the dark (blue) one are the hole pockets.

9 the calculated Fermi surfaces for both compounds in their calculated ground states. Note that while the calculated ground-state moment is *larger* than the experimental, the calculated number of carriers (the Fermi-surface volume) is also larger than the experimental one.^{38,39} Therefore it is hard to say what would be a better calculation to use for the transport properties: GGA gives more correct (but still too large) volumes of the Fermi surfaces while LDA gives more correct (but still too large) magnetic moments. Besides, as we will show next, the calculated anisotropy is very sensitive to these details, primarily because of the small size and the complicated shape of the Fermi surfaces. That is to say, the computational results should be taken with a large grain of salt and even if they provide in some aspects reasonable quantitative agreement with the experiment, this is likely fortuitous and one should not be tempted to use the calculated numbers any more than a qualitative guide.

Nevertheless, one can readily make some qualitative observations: first, both electron and hole Fermi surfaces

TABLE I. Calculated total and partial (hole, electrons) squared plasma frequencies in eV^2 . The x axis is parallel to the crystallographic a_o axis and perpendicular to the ferromagnetic chain direction. The second column indicates the calculated magnetic moment in μ_B/Fe .

	M	ω_{px}^2	ω_{py}^2	$\omega_{px}^2(h)$	$\omega_{py}^2(h)$	$\omega_{px}^2(e)$	$\omega_{py}^2(e)$
Ca122 (GGA)	1.85	0.36	0.37	0.14	0.24	0.22	0.14
Ca122 (LDA)	1.61	0.46	0.42	0.11	0.24	0.35	0.18
Ba122 (GGA)	1.96	0.42	0.32	0.13	0.13	0.29	0.19
Ba122 (LDA)	1.64	0.41	0.36	0.20	0.17	0.20	0.20

strongly violate the tetragonal symmetry; second, the two compounds differ substantially (this has been noticed before⁴⁰ and ascribed to the direct As-As overlap across the Ca plane). One can naively think that the calculated in-plane transport anisotropy should be very large. For instance, the authors of Ref. 15, having observed a strong violation of the tetragonal symmetry in their scanning tunnel microscope experiment, consistent with Fermi-surface topology shown in Fig. 9, concluded that a single-domain material will be essentially one dimensional. As we see, this appears not to be the case either in experiment or in theory (Table I). Particularly, in the antiferromagnetic LDA ground-state Ca122 has an anisotropy σ_{xx}/σ_{yy} of 1.10(+10%), and in the GGA ground state 0.97(-3%). In Ba122 the corresponding numbers are +14% and +31%.

Interestingly, the reason for such low anisotropy is different for the two compounds. As one can see from the Table I, in Ca122 the holes and the electrons separately have noticeable anisotropies of the opposite sign: -42% and +57%, respectively, in GGA, and -46% and +94% in LDA. The net anisotropy is thus small owing to the large cancellation of these two terms. This cancellation holds only if the relaxation times for holes and electrons are similar. The validity of this approximation in Ca122 is unknown but in Ba122 it is known to be highly questionable. Based on the Hall-effect data, it was argued^{38,39} that the electrical transport in Ba122 at low temperatures is dominated by electrons.

On the other hand, in Ba122 both the holes and electrons separately show rather weak anisotropy of the same sign, especially in LDA: 18% for the holes and 0% for the electrons. In GGA, these numbers are 0% and +52%. The reason is that while the Fermi-surface pockets in Ba122 are aligned along x , violating the tetragonal symmetry, each of these pockets separately (and as opposed to Ca122) shows relatively little anisotropy.

While these numbers are not quantitatively reliable, they show two qualitative trends observed in the experiment: first, despite the fact that the Fermi surfaces themselves are strongly anisotropic, the transport anisotropy is weak in Ca122 and moderate in Ba122. Second, despite the fact that the magnetic structure suggests much higher conductivity along y (i.e., along the ferromagnetic chains) than along x , the opposite holds both in the calculations (although within the computational uncertainty one cannot insist on any given sign) and in the experiment.

The temperature dependence is more intriguing. Obviously, if one could plot the anisotropy as a function of the long-range staggered magnetization, it has to be finite when

the magnetization is maximal, at $T=0$, and zero when the magnetization is vanishingly small. Yet in the experiment the anisotropy is growing with temperature while the moment decreases. This means that right below T_{TO} the magnetic moments are already large, even though incompletely ordered (as oppose to what the spin-Peierls model^{41,42} would imply) and so is the transport anisotropy. An example of such model is the dynamic domain scenario²³ that suggests that the long-range order is destroyed primarily by fluctuating domain walls that affect the average long-range magnetization but do not affect electronic anisotropy [see Fig. 1a in Ref. 23].

Within this scenario we can understand why the anisotropy experiences a nearly finite jump below T_{TO} , however, one needs to explain why the anisotropy actually decreases with cooling. One possible explanation is that the ratio of the plasma frequencies nonmonotonically depends on the magnitude of the magnetic moment. In this case anisotropy will be correlated with the moment for very small (experimentally inaccessible) magnetization but anticorrelated with the moment at larger moments.

Moreover, the fluctuating domain picture provides a natural explanation of why the conductivity is higher along the AFM direction. Indeed, as discussed in Ref. 23, there are two types of domains in these materials, twin domains and antiphase domains. Our method allows to get rid of twins but the antiphase domain walls, which do not couple to strain, are unaffected by our experimental procedure. As one can see in Fig. 1b in Ref. 23, the twin domain walls are symmetric, that is to say, have the same microscopic structure whether they run along x or along y , therefore as scatterers they would be isotropic. On the contrary, antiphase domains [Fig. 1b in Ref. 23] are very different: those perpendicular to the FM directions represent a change in the AFM pattern (local magnetic pattern is checkerboard rather than stripes) while those along the FM directions create a magnetic double stripe, which in 122 compounds has a very high-energy cost (both in the LDA calculations and in the J_1/J_2 model). Thus one expects a much higher density of the former antiphase walls than of the latter. Now we observe that the former type of walls strongly disrupt the current flowing perpendicular to them, i.e., along the FM direction and hardly disrupt the current flowing in the AFM direction. The opposite is true for the walls of the opposite orientation but, as discussed, concentration of such walls in thermodynamical equilibrium must be small.

Alternatively, one may think that if the hole and the electron anisotropies have opposite signs, the net anisotropy is

defined by their incomplete cancellation. In this case the observed temperature dependence is defined by the temperature dependence of the τ_h/τ_e ratio, which, of course, can have virtually any temperature dependence. This latter scenario is corroborated by the calculations in Ca122 but not in Ba122. One has to remember, as we mentioned before, that these calculations are not to be trusted on a quantitative level.

IV. CONCLUSIONS

In conclusion, we performed reversible mechanical detwinning of single-crystal CaFe_2As_2 and BaFe_2As_2 . The single-domain state was confirmed by direct polarized light imaging in both compounds and with high-energy x rays in BaFe_2As_2 . In both materials we find that the resistive anisotropy is largest at T_{TO} with $\rho_{aa}/\rho_{bb} \approx 1.2$ in Ca122 and ≈ 1.5 in Ba122. For Ca122 this anisotropy only exists below T_{TO} and diminishes upon further cooling, reaching about 1.05 at $T \sim 50$ K and remaining around that value at lower temperatures. For Ba122 the anisotropy exists both below and above T_{TO} , reflecting nematic fluctuations above T_{TO} and the second-order character of the phase transition there. The temperature dependence of the anisotropy is weaker in Ba122, the low-temperature value being comparable with the high-temperature one, 1.4 vs 1.5.

These results are rather counterintuitive in several aspects. First, if one adapts a simple Jahn-Teller-type orbital ordering picture,^{43–46} one expects that conductivity along the ferromagnetic “metallic” chains (y) should be higher than along the antiferromagnetic “insulating” direction (x). The opposite is true. Second, given the drastic anisotropy of the band structure and the Fermi surfaces (including the fully broken symmetry between the xz and yz orbitals), as confirmed by first-principles calculations, one expects a dramatic anisotropy while in fact we observe weak to moderate anisotropy, not atypical for many metals. Third, within the experimental accuracy, the maximal anisotropy is right below the transition and not when the order parameter (magnetic moment or the orthorhombicity) is maximal. Finally, despite the fact that

the degree of orthorhombicity and the magnetic order parameter monotonically *decrease* with temperature, the transport anisotropy actually *increases*.

The first two findings are fully corroborated by the first-principles calculations. These predict the correct (counterintuitive) sign of the anisotropy and a relatively moderate anisotropy magnitude. The third might reflect the existence of dynamic domains (similar to the nematic fluctuations) right below T_{TO} in Ca122, and both below and above in Ba122. In that case, the antiphase domain walls, as described in Ref. 23, break the long-range order without destroying the transport anisotropy. Such antiphase domain walls, as opposed to twin domain walls, are not eliminated in our sample because they do not couple to strain. These walls are natural scatterers for electrons moving along the FM directions, y , but not those moving along x , which readily explains the observed sign of the transport anisotropy.

As to the temperature dependence, we have no preferable interpretation of this effect; the most plausible cause seems to be the temperature dependence of the relaxation rates, which are known to change by more than an order of magnitude between $T=0$ and $T=T_{\text{TO}}$.

While this paper was prepared for submission, a preprint appeared reporting a partial mechanical detwinning using uniaxial stress in $\text{Ba}(\text{Fe}_{1-x}\text{Co}_x)_2\text{As}_2$.⁴⁷ The reported resistivity data for the parent BaFe_2As_2 are similar to those found in our study.

ACKNOWLEDGMENTS

We thank D. Robinson for the excellent support of the high-energy x-ray scattering study and L. Podervyansky for help in writing the manuscript. Use of the Advanced Photon Source was supported by the U.S. Department of Energy, Office of Science, under Contract No. DE-AC02-06CH11357. Work at the Ames Laboratory was supported by the U.S. Department of Energy, Office of Basic Energy Sciences, Division of Materials Sciences and Engineering under Contract No. DE-AC02-07CH11358. R.P. acknowledges support from Alfred P. Sloan Foundation.

*Corresponding authors.

†tanatar@ameslab.gov

‡prozorov@ameslab.gov

¹Y. Kamihara, T. Watanabe, M. Hirano, and H. Hosono, *J. Am. Chem. Soc.* **130**, 3296 (2008).

²M. Rotter, M. Tegel, and D. Johrendt, *Phys. Rev. Lett.* **101**, 107006 (2008).

³M. S. Torikachvili, S. L. Bud'ko, N. Ni, and P. C. Canfield, *Phys. Rev. Lett.* **101**, 057006 (2008).

⁴C. de la Cruz, Q. Huang, J. W. Lynn, J. Y. Li, W. Ratcliff, J. L. Zarestky, H. A. Mook, G. F. Chen, J. L. Luo, N. L. Wang, and P. C. Dai, *Nature (London)* **453**, 899 (2008).

⁵M. A. Tanatar, A. Kreyssig, S. Nandi, N. Ni, S. L. Bud'ko, P. C. Canfield, A. I. Goldman, and R. Prozorov, *Phys. Rev. B* **79**, 180508(R) (2009).

⁶A. Subedi, D. J. Singh, and M. H. Du, *Phys. Rev. B* **78**, 060506(R) (2008).

⁷N. Ni, M. E. Tillman, J.-Q. Yan, A. Kracher, S. T. Hannahs, S. L. Bud'ko, and P. C. Canfield, *Phys. Rev. B* **78**, 214515 (2008).

⁸R. Prozorov, M. A. Tanatar, N. Ni, A. Kreyssig, S. Nandi, S. L. Bud'ko, A. I. Goldman, and P. C. Canfield, *Phys. Rev. B* **80**, 174517 (2009).

⁹S. Nandi, M. G. Kim, A. Kreyssig, R. M. Fernandes, D. K. Pratt, A. Thaler, N. Ni, S. L. Bud'ko, P. C. Canfield, J. Schmalian, R. J. McQueeney, and A. I. Goldman, *Phys. Rev. Lett.* **104**, 057006 (2010).

¹⁰B. Kalisky, J. Kirtley, J. Analytis, J. Chu, A. Vailionis, I. Fisher, and K. Moler, [arXiv:0906.5184](https://arxiv.org/abs/0906.5184) (unpublished).

¹¹J. G. Analytis, R. D. McDonald, J.-H. Chu, S. C. Riggs, A. F. Bangura, C. Kucharczyk, M. Johannes, and I. R. Fisher, *Phys.*

- Rev. B* **80**, 064507 (2009).
- ¹²D. Tompsett and G. Lonzarich, [arXiv:0902.4859](https://arxiv.org/abs/0902.4859) (unpublished).
- ¹³D. Kasinathan, A. Ormeci, K. Koch, U. Burkhardt, W. Schnelle, A. Leithe-Jasper, and H. Rosner, *New J. Phys.* **11**, 025023 (2009).
- ¹⁴A. F. Kemper, C. Cao, P. J. Hirschfeld, and H.-P. Cheng, *Phys. Rev. B* **80**, 104511 (2009).
- ¹⁵T.-M. Chuang, M. P. Allan, Jinho Lee, Yang Xie, Ni Ni, S. L. Bud'ko, G. S. Boebinger, P. C. Canfield, and J. C. Davis, *Science* **327**, 181 (2010).
- ¹⁶I. I. Mazin and J. Schmalian, *Physica C* **469**, 614 (2009).
- ¹⁷C. Fang, H. Yao, W.-F. Tsai, J. P. Hu, and S. A. Kivelson, *Phys. Rev. B* **77**, 224509 (2008).
- ¹⁸C. Xu, M. Muller, and S. Sachdev, *Phys. Rev. B* **78**, 020501(R) (2008).
- ¹⁹R. Fernandes, L. VanBebber, S. Bhattacharya, P. Chandra, V. Keppens, D. Mandrus, M. McGuire, B. Sales, A. Sefat, and J. Schmalian, [arXiv:0911.3084](https://arxiv.org/abs/0911.3084) (unpublished).
- ²⁰J. Giapintzakis, D. M. Ginsberg, and P.-D. Han, *J. Low Temp. Phys.* **77**, 155 (1989).
- ²¹J. Chu, J. Analytis, D. Press, K. De Greve, T. Ladd, Y. Yamamoto, and I. Fisher, [arXiv:0911.3878](https://arxiv.org/abs/0911.3878) (unpublished).
- ²²A. N. Lavrov, S. Komiya, and Y. Ando, *Nature (London)* **418**, 385 (2002).
- ²³I. I. Mazin and M. D. Johannes, *Nat. Phys.* **5**, 141 (2009).
- ²⁴N. Ni, S. Nandi, A. Kreyssig, A. I. Goldman, E. D. Mun, S. L. Bud'ko, and P. C. Canfield, *Phys. Rev. B* **78**, 014523 (2008).
- ²⁵A. I. Goldman, D. N. Argyriou, B. Ouladdiaf, T. Chatterji, A. Kreyssig, S. Nandi, N. Ni, S. L. Bud'ko, P. C. Canfield, and R. J. McQueeney, *Phys. Rev. B* **78**, 100506(R) (2008).
- ²⁶H. Schmid, E. Burkhardt, B. N. Sun, and J. P. Rivera, *Physica C* **157**, 555 (1989); U. Welp, M. Grimsditch, H. You, W. K. Kwok, M. M. Fang, G. W. Crabtree, and J. Z. Liu, *ibid.* **161**, 1 (1989).
- ²⁷M. A. Tanatar, N. Ni, S. L. Bud'ko, P. C. Canfield, and R. Prozorov, *Supercond. Sci. Technol.* **23**, 054002 (2010).
- ²⁸A. Kreyssig, S. Chang, Y. Janssen, J. W. Kim, S. Nandi, J. Q. Yan, L. Tan, R. J. McQueeney, P. C. Canfield, and A. I. Goldman, *Phys. Rev. B* **76**, 054421 (2007).
- ²⁹P. Blaha, K. Schwarz, G. K. H. Madsen, D. Kvasnicka, and J. Luitz, in *An Augmented Plane Wave Plus Local Orbitals Program for Calculating Crystal Properties*, edited by K. Schwarz (TU Wien, Austria, 2001).
- ³⁰The x-ray study of Ref. 5 revealed that despite small size, the domains propagate through the whole sample thickness and are of columnar type.
- ³¹M. S. Torikachvili, S. L. Bud'ko, N. Ni, P. C. Canfield, and S. T. Hannahs, *Phys. Rev. B* **80**, 014521 (2009).
- ³²M. A. Tanatar, N. Ni, G. D. Samolyuk, S. L. Bud'ko, P. C. Canfield, and R. Prozorov, *Phys. Rev. B* **79**, 134528 (2009).
- ³³S. R. Saha, N. P. Butch, K. Kirshenbaum, J. Paglione, and P. Y. Zavalij, *Phys. Rev. Lett.* **103**, 037005 (2009).
- ³⁴S. Diallo, D. Pratt, R. Fernandes, W. Tian, J. Zarestky, M. Lumsden, T. Perring, C. Broholm, N. Ni, S. Bud'ko, P. Canfield, H. Li, D. Vaknin, A. Kreyssig, A. Goldman, and R. McQueeney, [arXiv:1001.2804](https://arxiv.org/abs/1001.2804) (unpublished).
- ³⁵S. O. Diallo, V. P. Antropov, T. G. Perring, C. Broholm, J. J. Pulikkotil, N. Ni, S. L. Bud'ko, P. C. Canfield, A. Kreyssig, A. I. Goldman, and R. J. McQueeney, *Phys. Rev. Lett.* **102**, 187206 (2009).
- ³⁶J. Zhao, D. T. Adroja, D. X. Yao, R. Bewley, S. L. Li, X. F. Wang, G. Wu, X. H. Chen, J. P. Hu, and P. C. Dai, *Nat. Phys.* **5**, 555 (2009).
- ³⁷P. B. Allen, *Phys. Rev. B* **17**, 3725 (1978).
- ³⁸L. Fang, H. Luo, P. Cheng, Z. Wang, Y. Jia, G. Mu, B. Shen, I. I. Mazin, L. Shan, C. Ren, and H.-H. Wen, *Phys. Rev. B* **80**, 140508(R) (2009).
- ³⁹F. Rullier-Albenque, D. Colson, A. Forget, and H. Alloul, *Phys. Rev. Lett.* **103**, 057001 (2009).
- ⁴⁰T. Yildirim, *Phys. Rev. Lett.* **102**, 037003 (2009).
- ⁴¹A. V. Chubukov, D. V. Efremov, and I. Eremin, *Phys. Rev. B* **78**, 134512 (2008).
- ⁴²M. M. Korshunov, I. Eremin, D. V. Efremov, D. L. Maslov, and A. V. Chubukov, *Phys. Rev. Lett.* **102**, 236403 (2009); I. Eremin and A. V. Chubukov, *Phys. Rev. B* **81**, 024511 (2010).
- ⁴³F. Krüger, S. Kumar, J. Zaanen, and J. van den Brink, *Phys. Rev. B* **79**, 054504 (2009).
- ⁴⁴W. Lv, J. Wu, and P. P. Philip, *Phys. Rev. B* **80**, 224506 (2009).
- ⁴⁵R. Singh, [arXiv:0903.4408](https://arxiv.org/abs/0903.4408) (unpublished).
- ⁴⁶E. Bascones, M. Calderon, and B. Valenzuela, [arXiv:1002.2584](https://arxiv.org/abs/1002.2584) (unpublished).
- ⁴⁷J. Chu, J. Analytis, K. De Greve, P. McMahon, Z. Islam, Y. Yamamoto, and I. Fisher, [arXiv:1002.3364](https://arxiv.org/abs/1002.3364) (unpublished).